In Vivo Tumor Targeting and Image-Guided Drug Delivery with Antibody-Conjugated, Radiolabeled Mesoporous Silica Nanoparticles

Feng Chen,[†,▽] Hao Hong,[†,▽] Yin Zhang,[‡] Hector F. Valdovinos,[‡] Sixiang Shi,[§] Glen S. Kwon,[⊥] Charles P. Theuer,[∥] Todd E. Barnhart,[‡] and Weibo Cai[†,‡,§,#,*]

[†]Department of Radiology, University of Wisconsin—Madison, Wisconsin 53706, United States, [‡]Department of Medical Physics, University of Wisconsin—Madison, Wisconsin 53706, United States, [§]Materials Science Program, University of Wisconsin—Madison, Wisconsin 53706, United States, [⊥]Pharmaceutical Sciences Division, School of Pharmacy, University of Wisconsin—Madison, Wisconsin 53706, United States, [∥]TRACON Pharmaceuticals, Inc., San Diego, California 92122, United States, and [#]University of Wisconsin Carbone Cancer Center, Madison, Wisconsin 53706, United States. [▽]Feng Chen and Hao Hong contributed equally to this work

ABSTRACT Since the first use of biocompatible mesoporous silica ($mSiO_2$) nanoparticles as drug delivery vehicles, *in vivo* tumor targeted imaging and enhanced anticancer drug delivery has remained a major challenge. In this work, we describe the development of functionalized $mSiO_2$ nanoparticles for actively targeted positron emission tomography (PET) imaging and drug delivery in 4T1 murine breast tumor-bearing mice. Our structural design involves the synthesis, surface functionalization with thiol groups, PEGylation, TRC105 antibody (specific for CD105/endoglin) conjugation, and ^{64}Cu-labeling of uniform 80 nm sized $mSiO_2$ nanoparticles. Systematic *in vivo* tumor targeting studies clearly demonstrated that ^{64}Cu-NOTA-$mSiO_2$-PEG-TRC105 could accumulate prominently at the 4T1 tumor site *via* both the enhanced permeability and retention effect and TRC105-mediated binding to tumor vasculature CD105. As a proof-of-concept, we also demonstrated successful enhanced tumor targeted delivery of doxorubicin (DOX) in 4T1 tumor-bearing mice after intravenous injection of DOX-loaded NOTA-$mSiO_2$-PEG-TRC105, which holds great potential for future image-guided drug delivery and targeted cancer therapy.

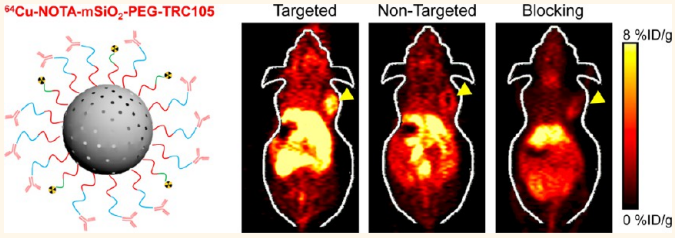

KEYWORDS: mesoporous silica ($mSiO_2$) nanoparticles · tumor angiogenesis · *in vivo* tumor targeting · positron emission tomography (PET) · drug delivery · theranostics

Over the past decade, tremendous efforts have been devoted to the design and functionalization of various types of nanoplatforms, such as iron oxide nanoparticles,[1] gold nanostructures,[2] carbon nanomaterials,[3,4] and upconversion nanoparticles,[5,6] which not only can be used for visualizing the tumors noninvasively with different imaging techniques, but also hold the potential for efficient tumor targeted delivery of anticancer drugs.[7,8] Uniform mesoporous silica ($mSiO_2$) nanoparticle is another category of such promising nanoplatforms and has drawn increasing interest recently because of its nontoxic nature, easily modifiable surface and good biocompatibility.[9,10] Because of their tailorable mesoporous structure, high specific surface area and large pore volume, $mSiO_2$ nanoparticles have many advantages over other drug delivery systems such as high drug loading capacity, controllable (or stimuli-responsive) drug release behavior, and codelivery capability.[11] Development and optimization of various strategies for improving the *in vivo* tumor specific targeting efficiency of various drug delivery systems (*e.g.*, $mSiO_2$ nanoparticles) is of critical importance, which remains a major challenge for future cancer targeted imaging and therapy. Although various targeting ligands (*e.g.*, folic acid,[12] transferrin,[13] aptamer[14] and herceptin[15]) have been conjugated to $mSiO_2$ nanoparticles, which exhibited *in vitro* tumor cell targeting and enhanced therapeutic efficacy, very limited progress has been achieved in extending such success into *in vivo* settings in animal models.[16,17]

* Address correspondence to wcai@uwhealth.org.

Received for review July 15, 2013 and accepted September 26, 2013.

Published online September 26, 2013
10.1021/nn403617j

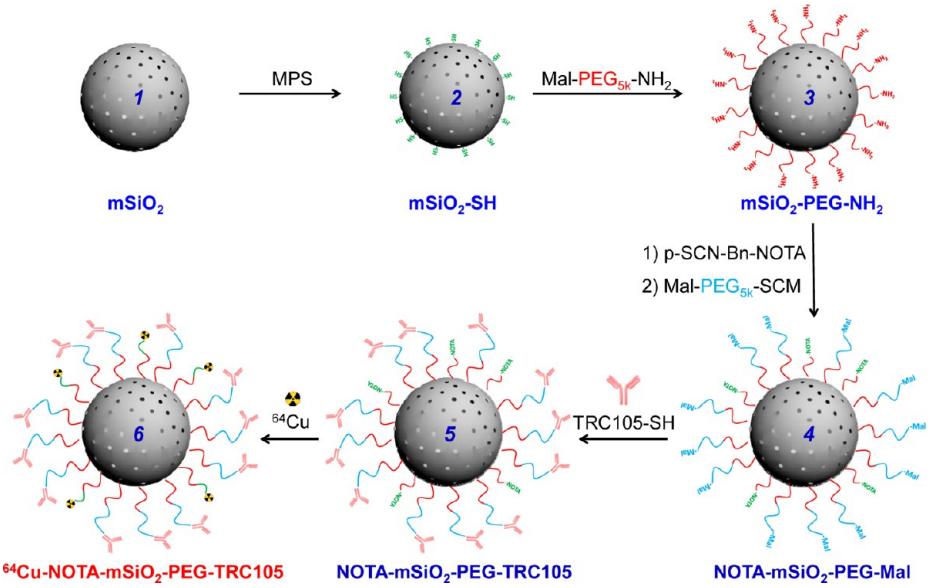

Scheme 1. A schematic illustration of the synthesis of ^{64}Cu-NOTA-mSiO$_2$-PEG-TRC105. Uniform mSiO$_2$ nanoparticles (1) were first modified with −SH groups to form mSiO$_2$−SH (2). mSiO$_2$−SH was PEGylated with Mal-PEG$_{5k}$-NH$_2$ to form mSiO$_2$-PEG-NH$_2$ (3), which was subjected to NOTA conjugation and subsequent PEGylation to yield NOTA-mSiO$_2$-PEG-Mal (4). NOTA-mSiO$_2$-PEG-TRC105 (5) could be obtained by reacting TRC105-SH with 4. ^{64}Cu-labeling was performed in the last step to generate ^{64}Cu-NOTA-mSiO$_2$-PEG-TRC105 (6).

The suboptimal performance of many nanoscale drugs *in vivo* is in large part due to inefficient drug delivery.[18,19] Currently, passive targeting based on the enhanced permeability and retention (EPR) effect remains the primary strategy for delivering drug-loaded mSiO$_2$ to tumor sites,[20−22] and progress in actively targeted drug delivery is slow and severely understudied. In one attempt to target folic acid-conjugated and fluorescein isothiocyanate (FITC) doped mSiO$_2$ to MCF-7 tumor-bearing nude mice, only marginal difference in tumor uptake of mSiO$_2$ could be observed, which is likely due to the high tissue autofluorescence (which interferes with the signal originated from FITC) and limited targeting efficiency of such tumor cell-based targeting strategy.[16] Because of the relatively short blood circulation lifetime, imperfect surface conjugation chemistry, lack of specific tumor (or tumor vasculature) targeting, and limited extravasation, the development of an optimal targeted drug delivery system based on mSiO$_2$ is urgently needed in the field.

Tumor vasculature targeting can be a more efficient strategy since, unlike tumor cell-based targeting, extravasation is not required to observe the tumor signal.[23−25] Angiogenesis, the formation of new blood vessels from preexisting vasculature, is essential for tumor growth and progression.[26,27] CD105 (also called endoglin) is an ideal marker for tumor angiogenesis, which is almost exclusively expressed on proliferating endothelial cells.[28,29] Various literature reports have demonstrated that the expression level of CD105 is correlated with poor prognosis in more than 10 solid tumor types,[30] which makes it an extremely attractive and universal vascular target for solid tumors. Using TRC105 (a human/murine chimeric IgG1 monoclonal antibody, which binds to both human and murine CD105[31]) as the targeting moiety, we reported the first positron emission tomography (PET) imaging of CD105 expression in a mouse model of breast cancer,[32,33] and subsequently confirmed high CD105-mediated uptake of radiolabeled TRC105 in a number of xenograft tumor models (*e.g.*, triple-negative breast cancer, pancreatic cancer, prostate cancer, and brain tumor), demonstrating broad potential for future applications of CD105-targeted agents in cancer imaging and therapy.[34]

In this work, we aim to develop a surface functionalized mSiO$_2$ for *in vivo* tumor (vasculature) targeted imaging and improved drug delivery efficiency. Uniform mSiO$_2$ nanoparticles were synthesized using a well-established soft-template method,[35] and subsequently conjugated to TRC105 and (*S*)-2-(4-isothiocyanatobenzyl)-1,4,7-triazacyclononane-1,4,7-triacetic acid (*i.e.*, *p*-SCN-Bn-NOTA) through polyethylene glycol (PEG) linkers, which was then labeled with ^{64}Cu ($t_{1/2}$: 12.7 h) to form the ^{64}Cu-NOTA-mSiO$_2$-PEG-TRC105 nanoconjugate (Scheme 1). Systematic *in vivo* PET imaging, biodistribution, and blocking studies were performed in 4T1 murine breast tumor-bearing mice to evaluate and confirm their tumor specific targeting capability, which was validated by various *in vitro* and *ex vivo* experiments. In our previous reports, it has been demonstrated that CD105 was expressed at a high level on actively proliferating tumor vasculature, but at a very low level in the normal organs or the 4T1 tumor cells.[24,32,33,36] As a proof-of-concept, we also demonstrated the enhanced tumor-targeted delivery efficiency of doxorubicin (DOX, a commonly used

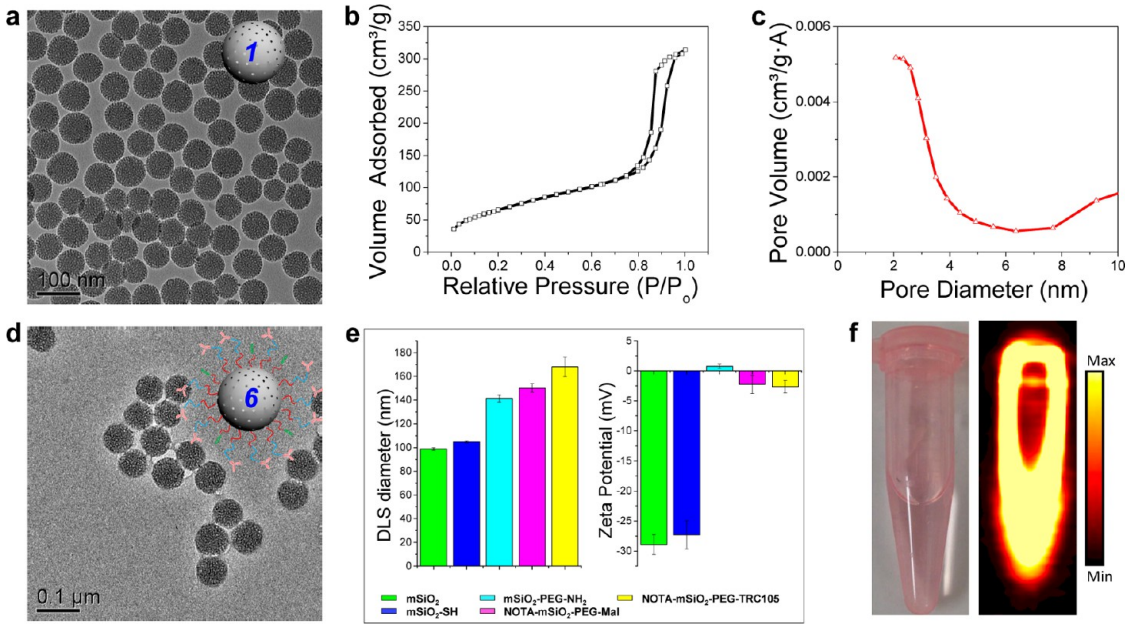

Figure 1. (a) A TEM image of $mSiO_2$ before surface modification. (b) Nitrogen adsorption−desorption isotherms and (c) the corresponding pore size distribution of $mSiO_2$ nanoparticles. (d) A TEM image of NOTA-$mSiO_2$-PEG-TRC105 in PBS solution. (e) DLS size (left) and zeta potential (right) changes of $mSiO_2$ after step-by-step surface modification. (f) A digital photo (left) and PET phantom image (right) of ^{64}Cu-NOTA-$mSiO_2$-PEG-TRC105 nanoparticle in PBS solution.

anticancer drug) in 4T1 tumor-bearing mice after intravenous injection of DOX-loaded NOTA-$mSiO_2$-PEG-TRC105 nanoparticles, which holds great potential for future image-guided drug delivery and targeted cancer therapy.

RESULTS

Synthesis and Characterization of NOTA-$mSiO_2$-PEG-TRC105. Scheme 1 shows the major steps toward the synthesis of ^{64}Cu-NOTA-$mSiO_2$-PEG-TRC105. As-synthesized uniform $mSiO_2$ nanoparticles (**1**) were first functionalized with thiol groups (−SH) with (3-mercaptopropyl)trimethoxysilane (MPS) to form $mSiO_2$−SH (**2**), followed by PEGylation with Mal-PEG_{5k}-NH_2 (Mal denotes maleimide) to obtain $mSiO_2$-PEG-NH_2 (**3**), leaving amino (−NH_2) groups on the surface for further conjugations. Desired amount of *p*-SCN-Bn-NOTA was then added to obtain NOTA-$mSiO_2$-PEG-NH_2. Afterward, another heterobifunctional PEG (Mal-PEG_{5k}-SCM, SCM denotes succinimidyl carboxy methyl ester) was used to generate NOTA-$mSiO_2$-PEG-Mal (**4**), which was reacted with TRC105-SH to yield NOTA-$mSiO_2$-PEG-TRC105 (**5**). Lastly, the NOTA-$mSiO_2$-PEG-TRC105 was labeled with ^{64}Cu to form the ^{64}Cu-NOTA-$mSiO_2$-PEG-TRC105 nanoconjugate (**6**).

Uniform $mSiO_2$ nanoparticles with an average particle size of 80 nm were synthesized following the literature procedure.[35] Figure 1a shows the representative transmission electron microscopy (TEM) image of as-prepared $mSiO_2$ with wormlike mesoporous structures. The size of $mSiO_2$ could easily be tuned simply by changing the amount of triethanolamine used, as shown in Figure S1, Supporting Information. Fourier transform infrared spectroscopy was performed to confirm the successful removal of surfactant hexadecyl trimethyl ammonium chloride (CTAC), as evidenced by the absence of characteristic C−H peak in the 3000−2800 cm^{-1} range for surfactant-extracted $mSiO_2$ (Figure S2, Supporting Information).[35] Nitrogen adsorption−desorption isotherm results indicated that the $mSiO_2$ nanoparticles possess relatively high specific surface areas of 238 m^2/g and well-defined pore sizes of ∼2.2 nm (Figure 1b and c).

No obvious changes in the morphology of $mSiO_2$ were observed after surface modifications, as evidenced by TEM images in Figure 1d and Figure S3b, Supporting Information. The successful surface modifications were further confirmed by dynamic light scattering (DLS) and zeta potential measurements, as shown in Figure 1e and Figure S3c, Supporting Information. In comparison with sizes observed from TEM images, the diameters of $mSiO_2$ nanoparticles based on DLS after step-by-step modifications became larger to varied extent because of the presence of hydrated layers, PEG chains, and TRC105. No obvious change of surface charge (from −28.9 ± 1.7 mV to −27.3 ± 2.4 mV) was observed after −SH modification of $mSiO_2$, which changed significantly to 0.8 ± 0.4 mV after conjugation with Mal-PEG_{5k}-NH_2, indicating successful coating with the PEG layer. The $mSiO_2$-PEG-NH_2 could be well-dispersed in PBS solution (pH = 7.4) without any obvious aggregation for several weeks (Figure S4, Supporting Information), which further confirmed successful PEGylation. The final DLS diameter and surface

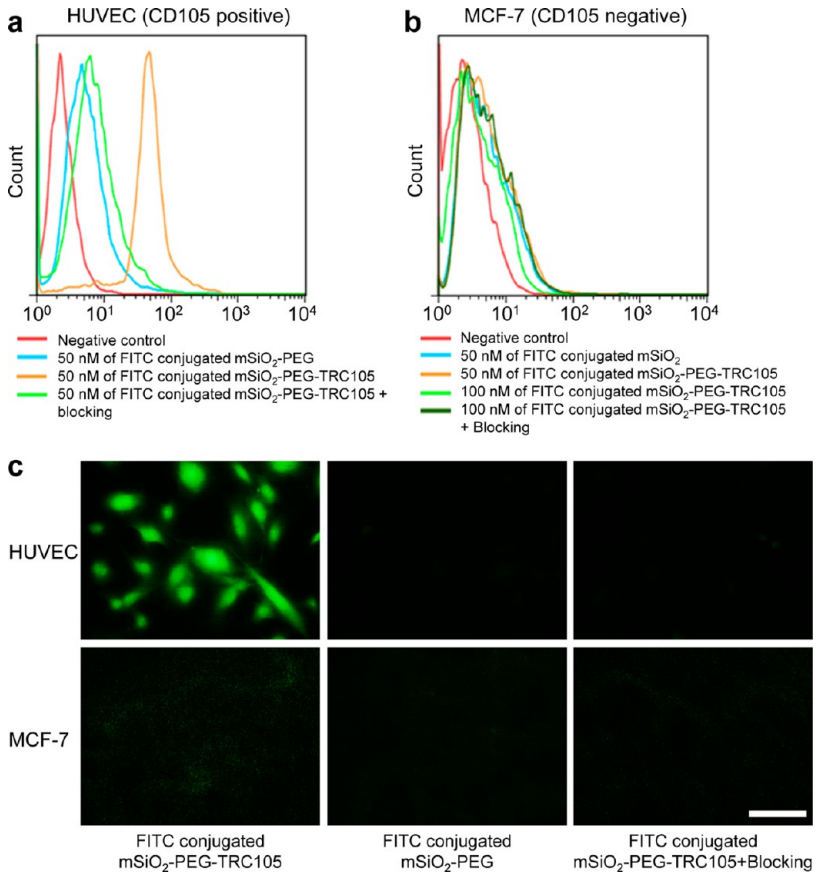

Figure 2. ***In vitro*** **investigation of $mSiO_2$ conjugates. Flow cytometry analysis of $mSiO_2$ conjugates in (a) HUVEC (CD105 positive) and (b) MCF-7 (CD105 negative) cells after 15 min incubation and subsequent washing. (c) Representative fluorescence images of HUVECs and MCF-7 cells stained with FITC conjugated $mSiO_2$-PEG-TRC105, FITC conjugated $mSiO_2$-PEG, or FITC conjugated $mSiO_2$-PEG-TRC105 with a blocking dose of TRC105. Scale bar: 50 μm.**

charge of NOTA-$mSiO_2$-PEG-TRC105 were found to be 168.0 $\pm$ 8.2 nm and -2.7 ± 1.0 mV, respectively. Taken together, these data confirmed the successful surface modifications of as-synthesized $mSiO_2$ nanoparticles to the NOTA-$mSiO_2$-PEG-TRC105 nanoconjugate.

In Vitro **CD105 Targeting.** To assess CD105-targeting efficiency of the $mSiO_2$ conjugates, human umbilical vein endothelial cells (HUVECs, CD105 positive) and MCF-7 human breast cancer cells (CD105 negative) were used for flow cytometry and fluorescence microscopy studies. FITC was conjugated to the surface of nanoparticles to form FITC conjugated $mSiO_2$-PEG-TRC105 and FITC conjugated $mSiO_2$-PEG to facilitate such investigation. The flow cytometry results from Figure 2a indicated that incubation with FITC conjugated $mSiO_2$-PEG-TRC105 could significantly enhance the mean fluorescence intensity of HUVECs (51.8-fold higher than the unstained cells), while treatment with FITC conjugated $mSiO_2$-PEG, or FITC conjugated $mSiO_2$-PEG-TRC105 with a blocking dose of TRC105 (500 μg/mL), only gave slight fluorescence enhancement (4.3-fold and 4.8-fold, respectively). Prolonging the incubation time from 15 min to 2 h did not improve the targeting efficiency significantly, as evidenced in Figure S5, Supporting Information, indicating rapid and highly efficient *in vitro* CD105 targeting.

In stark contrast, incubating FITC conjugated $mSiO_2$-PEG-TRC105 or FITC conjugated $mSiO_2$-PEG with MCF-7 cells only showed background fluorescence level for all groups (Figure 2b), demonstrating low nonspecific binding of functionalized $mSiO_2$ conjugates in CD105 negative cells. Fluorescence microscopy images exhibited similar trends as that observed in flow cytometry studies and provided visual evidence, showing strong green fluorescence in HUVECs when treated with FITC conjugated $mSiO_2$-PEG-TRC105 and extremely low level of fluorescence in all other groups (Figure 2c). Overall, these *in vitro* results demonstrated that FITC conjugated $mSiO_2$-PEG-TRC105 exhibited strong and specific binding to CD105-postive cells with negligible nonspecific binding, which warranted further *in vivo* investigation of NOTA-$mSiO_2$-PEG-TRC105.

Radiolabeling and Stability Evaluation. NOTA-$mSiO_2$-PEG-TRC105 and NOTA-$mSiO_2$-PEG were labeled with ^{64}Cu for *in vivo* studies. ^{64}Cu-NOTA-$mSiO_2$-PEG-TRC105 and ^{64}Cu-NOTA-$mSiO_2$-PEG were purified using PD-10 columns with PBS as the mobile phase. The radioactivity fractions (typically elute between 3.5 and 4.5 mL)

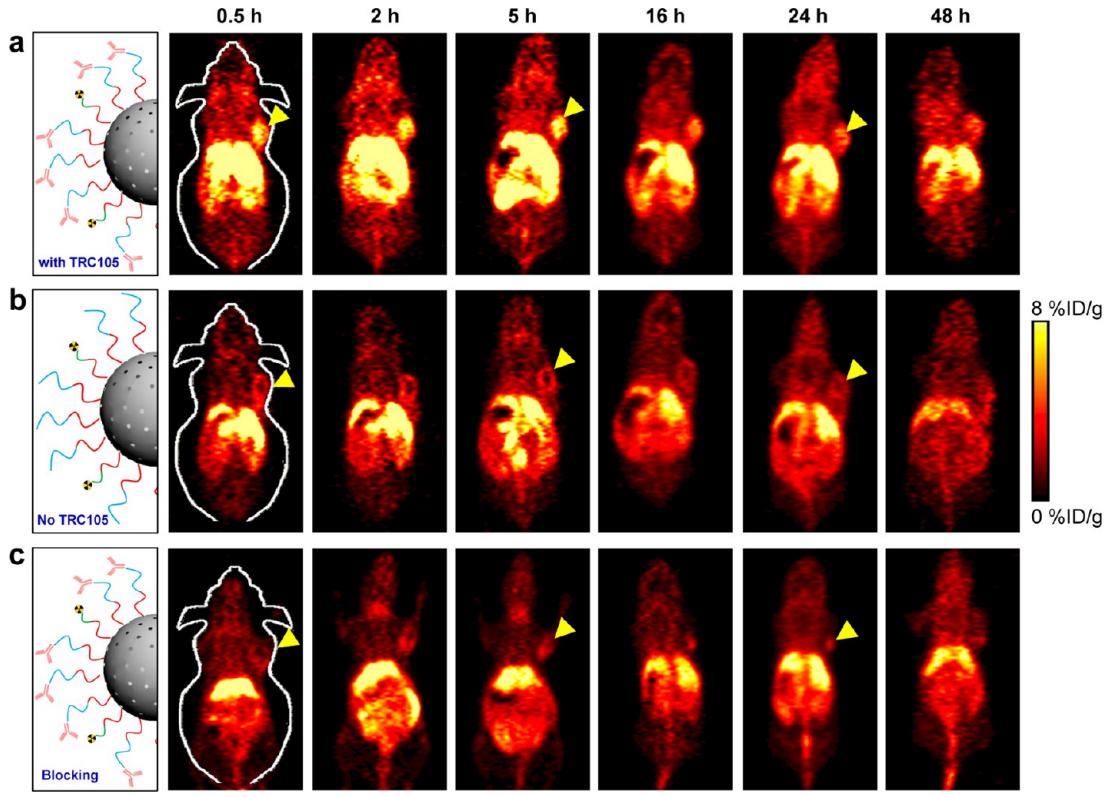

Figure 3. Serial coronal PET images of 4T1 tumor-bearing mice at different time points postinjection of (a) ^{64}Cu-NOTA-mSiO$_2$-PEG-TRC105, (b) ^{64}Cu-NOTA-mSiO$_2$-PEG, or (c) ^{64}Cu-NOTA-mSiO$_2$-PEG-TRC105 with a blocking dose of TRC105. Tumors were indicated by yellow arrowheads.

were collected for further *in vivo* experiments, and a typical size exclusion column chromatography profile can be seen in Figure S6, Supporting Information. After 6 mL of PBS, the unreacted ^{64}Cu may start to elute from the column. The decay-corrected radiochemical yield was >50% for both conjugates, based on 0.18 nmol of NOTA-mSiO$_2$-PEG-TRC105 (or NOTA-mSiO$_2$-PEG) per 37 MBq of ^{64}Cu, with radiochemical purity of >95%. Figure 1f shows a digital photo and a PET phantom image of ^{64}Cu-NOTA-mSiO$_2$-PEG-TRC105 in PBS solution, which demonstrated successful labeling of ^{64}Cu. The specific activity of both NOTA-mSiO$_2$-PEG-TRC105 and NOTA-mSiO$_2$-PEG was ~100 MBq/nmol, assuming complete recovery of NOTA-mSiO$_2$-PEG-TRC105 and NOTA-mSiO$_2$-PEG after size-exclusion chromatography.

Before *in vivo* investigation, serum stability studies were carried out to ensure that ^{64}Cu-NOTA-mSiO$_2$-PEG-TRC105 and ^{64}Cu-NOTA-mSiO$_2$-PEG are sufficiently stable for imaging purposes. It was found that more than 90% of ^{64}Cu remained within the mSiO$_2$ conjugates over a 48 h incubation period (Figure S7, Supporting Information), indicating high stability of the ^{64}Cu-NOTA complex. Since PET imaging detects the radioisotopes (*e.g.*, ^{64}Cu in this work) rather than the mSiO$_2$ conjugates themselves, excellent stability is a prerequisite for PET to reflect the *in vivo* distribution of ^{64}Cu-labeled mSiO$_2$ conjugates.

***In Vivo* Tumor Targeting and PET Imaging.** The time points of 0.5, 2, 5, 16, 24, and 48 h postinjection (p.i.) were chosen for serial PET scans. The coronal slices that contain the 4T1 tumors are shown in Figure 3. Quantitative data obtained from region-of-interest (ROI) analysis of the PET images are shown in Figure 4a–d. In addition, a representative PET/CT image of 4T1 tumor-bearing mice at 5 h p.i. of ^{64}Cu-NOTA-mSiO$_2$-PEG-TRC105, as well as coronal PET slices of mice in different groups at 5 h p.i., are shown in Figure 4e for direct visual comparison.

The liver uptake of ^{64}Cu-NOTA-mSiO$_2$-PEG-TRC105 was found to be 22.2 ± 0.8 %ID/g at 0.5 h p.i. and decreased gradually to 11.8 ± 2.4 %ID/g at 48 h p.i. (n = 3; Figure 4a, Table S1, Supporting Information), which is expected for intravenously injected nanomaterials. Importantly, accumulation of ^{64}Cu-NOTA-mSiO$_2$-PEG-TRC105 in the tumor occurred very quickly, which could be clearly visible at 0.5 h p.i. (5.7 ± 0.3 %ID/g) and peaked at around 5 h p.i. (5.9 ± 0.4 %ID/g), as shown in Figures 3a and 4a. In contrast, without the conjugation of TRC105, the 4T1 tumor uptake of either free ^{64}Cu (n = 2; Figure S8, Table S2, Supporting Information) or ^{64}Cu-NOTA-mSiO$_2$-PEG was found to be significantly lower than that of ^{64}Cu-NOTA-mSiO$_2$-PEG-TRC105 at all time points examined (n = 3; Figure 4b, Table S3, Supporting Information), indicating that TRC105 conjugation was the controlling factor for enhanced tumor uptake of ^{64}Cu-NOTA-mSiO$_2$-PEG-TRC105.

To further confirm CD105 specificity of ^{64}Cu-NOTA-mSiO$_2$-PEG-TRC105 *in vivo*, blocking studies were

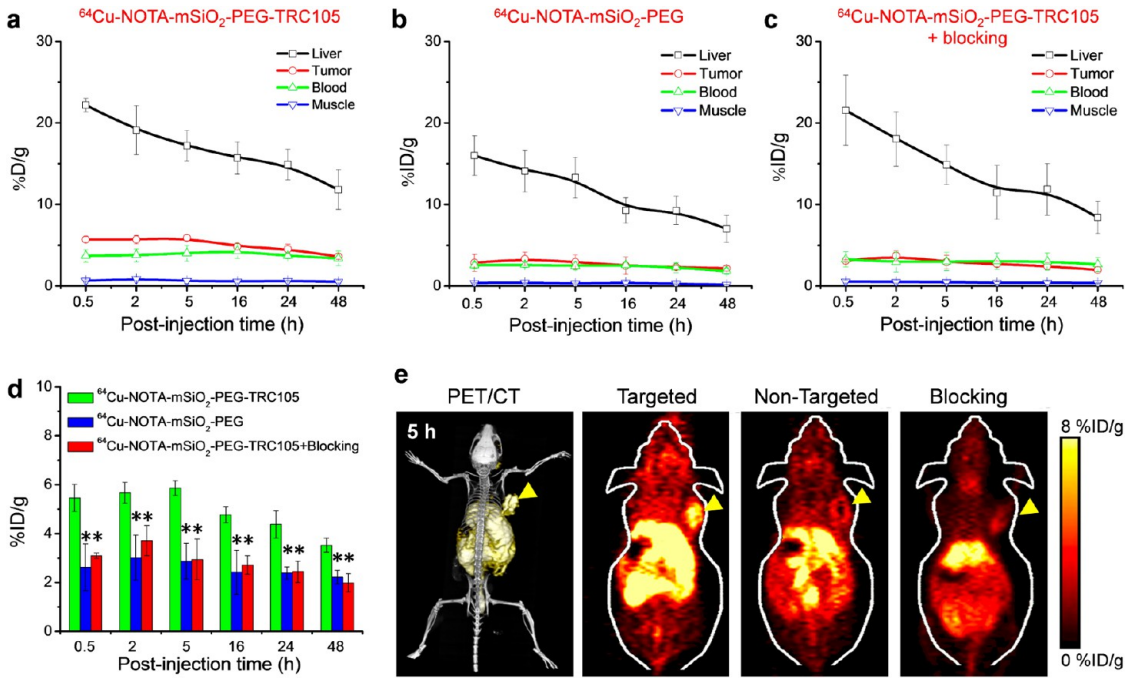

Figure 4. Quantitative analysis of the PET data. Time-activity curves of the liver, 4T1 tumor, blood, and muscle upon intravenous injection of (a) ^{64}Cu-NOTA-mSiO$_2$-PEG-TRC105, (b) ^{64}Cu-NOTA-mSiO$_2$-PEG, or (c) ^{64}Cu-NOTA-mSiO$_2$-PEG-TRC105 after a blocking dose of TRC105. (d) Comparison of 4T1 tumor uptake in the three groups. The difference between 4T1 tumor uptake of ^{64}Cu-NOTA-mSiO$_2$-PEG-TRC105 and the two control groups were statistically significant ($P < 0.05$) in all cases. (e) Representative PET/CT and PET images of mice in the three groups at 5 h postinjection. All data represent 3 mice per group.

performed. It was found that administration of a blocking dose (1 mg/mouse) of TRC105 at 1 h before ^{64}Cu-NOTA-mSiO$_2$-PEG-TRC105 injection could significantly reduce the tumor uptake to 2.9 ± 0.8 %ID/g at 5 h p.i. (n = 3, Figures 3c and 4c, Table S4, Supporting Information), demonstrating CD105 specificity of ^{64}Cu-NOTA-mSiO$_2$-PEG-TRC105 *in vivo*. Of note, the liver uptake and radioactivity in blood were not significantly affected by the blocking dose of TRC105, as shown in Figures 3c and 4c.

Figure 4d summarizes the 4T1 tumor uptake of the mSiO$_2$ conjugates in all three groups over time, where ^{64}Cu-NOTA-mSiO$_2$-PEG-TRC105 shows the highest tumor uptake throughout the study period ($P < 0.05$ in all cases, n = 3). Overall, aside from differences in tumor uptake, conjugation of TRC105 or administration of a blocking dose of TRC105 did not change the *in vivo* kinetics of these mSiO$_2$ conjugates in 4T1 tumor-bearing mice, which indicated that CD105 binding is responsible for the enhanced tumor uptake ^{64}Cu-NOTA-mSiO$_2$-PEG-TRC105 over the two control groups.

***Ex Vivo* Biodistribution Studies.** The biodistribution data of the mSiO$_2$ conjugates at 5 h (using a separate cohort of 3 mice) and 48 h p.i. (after the last PET scans) are shown in Figure 5, which matched very well with the PET data. Besides the liver, the kidney and intestine also had significant uptake of ^{64}Cu-NOTA-mSiO$_2$-PEG-TRC105 at 5 h p.i., at 7.2 ± 1.1 %ID/g and 9.4 ± 2.1 %ID/g, respectively (Figure 5a, n = 3). Aside from these organs that are responsible for clearance (*i.e.*, liver, kidney, intestine), the tumor uptake (5.4 ± 0.4 %ID/g, n = 3) of ^{64}Cu-NOTA-mSiO$_2$-PEG-TRC105 was higher than all other major organs, thus providing good tumor contrast with a tumor/muscle ratio of 6.2 ± 1.8 at 5 h p.i. and 3.5 ± 1.2 at 48 h p.i. (n = 3). In comparison with ^{64}Cu-NOTA-mSiO$_2$-PEG-TRC105, ^{64}Cu-NOTA-mSiO$_2$-PEG had slightly increased uptake in the liver (19.0 ± 2.0 %ID/g, n = 3) and significantly decreased uptake in tumor (2.6 ± 0.2 %ID/g, n = 3), based on the biodistribution studies at 5 h p.i. For mice euthanized at 48 h p.i. after the last PET scans, tumor uptake of ^{64}Cu-NOTA-mSiO$_2$-PEG-TRC105 was lower than that of 5 h p.i. but still remained prominent (Figure 5b). Overall, the PET and biodistribution data confirmed CD105 specificity of ^{64}Cu-NOTA-mSiO$_2$-PEG-TRC105 *in vivo*, and the corroborating results validated that serial PET imaging truly reflected the distribution pattern of mSiO$_2$ conjugates in tumor-bearing mice.

Histology. To further validate that tumor uptake of ^{64}Cu-NOTA-mSiO$_2$-PEG-TRC105 is CD105 specific and mSiO$_2$ conjugates were indeed delivered to the tumor, three 4T1 tumor-bearing mice were each injected with a larger dose of NOTA-mSiO$_2$-PEG-TRC105 (5 nmol/kg of mouse body weight) and euthanized at 0.5 and 5 h p.i. Tissues with significant uptake (*i.e.*, tumor, liver, spleen, and kidney) of ^{64}Cu-NOTA-mSiO$_2$-PEG-TRC105 were frozen for histological analysis. With negligible ^{64}Cu-NOTA-mSiO$_2$-PEG-TRC105 uptake, the muscle tissue was also examined as a normal control.

Of note, TRC105 within the NOTA-mSiO$_2$-PEG-TRC105 conjugate served as the primary antibody for

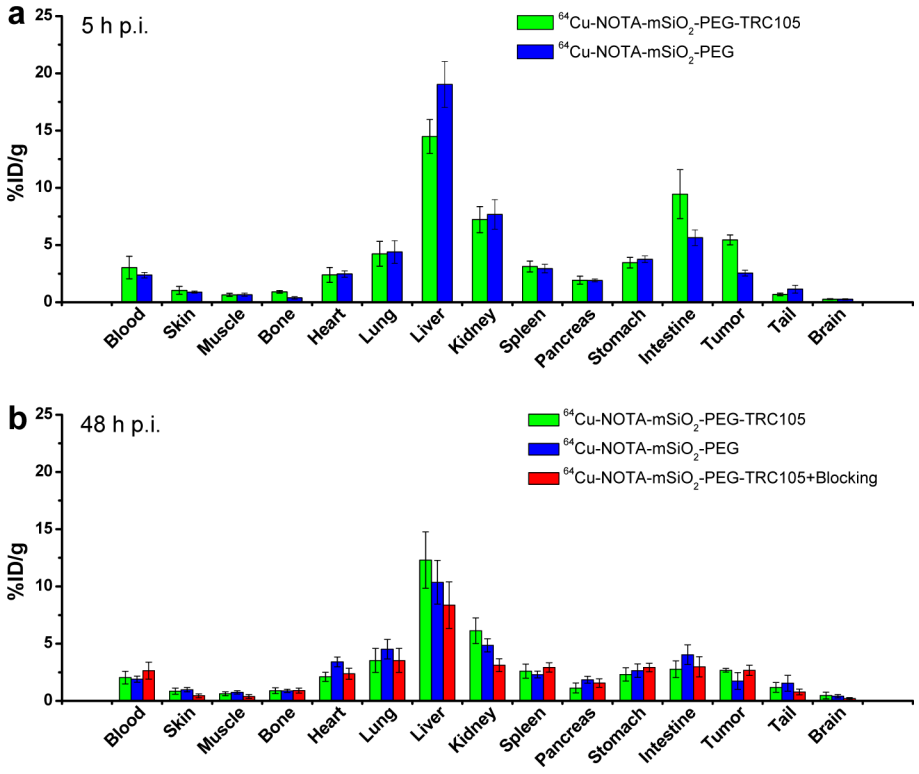

Figure 5. Biodistribution studies in 4T1 tumor-bearing mice. (a) Biodistribution of ^{64}Cu-NOTA-mSiO$_2$-PEG-TRC105 and ^{64}Cu-NOTA-mSiO$_2$-PEG in 4T1 tumor-bearing mice at 5 h postinjection. (b) Biodistribution of ^{64}Cu-NOTA-mSiO$_2$-PEG-TRC105, ^{64}Cu-NOTA-mSiO$_2$-PEG, and ^{64}Cu-NOTA-mSiO$_2$-PEG-TRC105 after a blocking dose of TRC105 in 4T1 tumor-bearing mice at 48 h postinjection. All data represent 3 mice per group.

histological analysis (*i.e.*, only fluorescently labeled antihuman IgG was used). Therefore, the green fluorescence signal from TRC105 in Figure 6 indicated the presence of NOTA-mSiO$_2$-PEG-TRC105. The histology data demonstrated that at 0.5 h p.i., NOTA-mSiO$_2$-PEG-TRC105 distribution in the 4T1 tumor was primarily on the tumor vasculature with little extravasation (indicated by the good overlay of red and green fluorescence signal, which represented CD31 and NOTA-mSiO$_2$-PEG-TRC105, respectively, Figure 6a). Significant extravasation of NOTA-mSiO$_2$-PEG-TRC105 at 5 h p.i. was also observed in the tumor tissue, where separation of the red and green fluorescence signals can be clearly seen (Figure 6b).

Prominent green fluorescence signal from the liver, kidney, and spleen slices indicated significant uptake of NOTA-mSiO$_2$-PEG-TRC105 in these three organs at 5 h p.i. (Figure 6 c–e), which corroborated the PET findings. The green fluorescence attributed to NOTA-mSiO$_2$-PEG-TRC105 exhibited weak overlay with CD31 staining of vessels, indicating that the uptake of NOTA-mSiO$_2$-PEG-TRC105 in those organs was most likely due to nonspecific capture by macrophages and/or other mechanisms that are not related to CD105 expression. No observable green fluorescence was detected in muscle (Figure 6f), which is consistent with the PET imaging results.

Enhanced Tumor Targeted Drug Delivery *in Vivo*. As a proof-of-concept, we further demonstrated the feasibility of enhanced tumor targeted drug delivery *in vivo* using TRC105 conjugated mSiO$_2$ loaded with an anticancer drug DOX, denoted as NOTA-mSiO$_2$(DOX)-PEG-TRC105. The loading capacity of DOX in mSiO$_2$ was estimated to range from 76.6 to 481.6 mg/g, as shown in Table S5, Supporting Information. UV–vis absorbance spectra of mSiO$_2$(DOX) exhibited characteristic absorption peak at around 480 nm (Figure 7a), which could give strong fluorescence signal under 465 nm excitation (Figure 7b), clearly indicating successful loading of DOX into the mSiO$_2$. A previous literature report has shown that the protonation of silanols (–Si–OH) in mSiO$_2$ with the decrease of pH could lead to a decrease in the electrostatic interaction between DOX and mSiO$_2$, causing the dissociation of DOX from the silica surface and mesoporous channels.[37] Such phenomenon was confirmed in our study: a pH-sensitive release profile was observed with much faster DOX release rate at pH 5.0 than that at pH 7.4 (Figure 7c).

To prepare NOTA-mSiO$_2$(DOX)-PEG-TRC105 for tumor targeted drug delivery, DOX was mixed with mSiO$_2$-PEG-NH$_2$ in PBS and kept under constant shaking for 24 h to form mSiO$_2$(DOX)-PEG-NH$_2$. Subsequently, similar protocols as shown in Scheme 1 were used for NOTA and TRC105 conjugation, forming NOTA-mSiO$_2$-(DOX)-PEG-TRC105. The final DOX concentration in both NOTA-mSiO$_2$(DOX)-PEG-TRC105 and NOTA-mSiO$_2$-(DOX)-PEG (suspended in PBS solution) were adjusted to 390 μg/mL, as evidenced by the optical images in

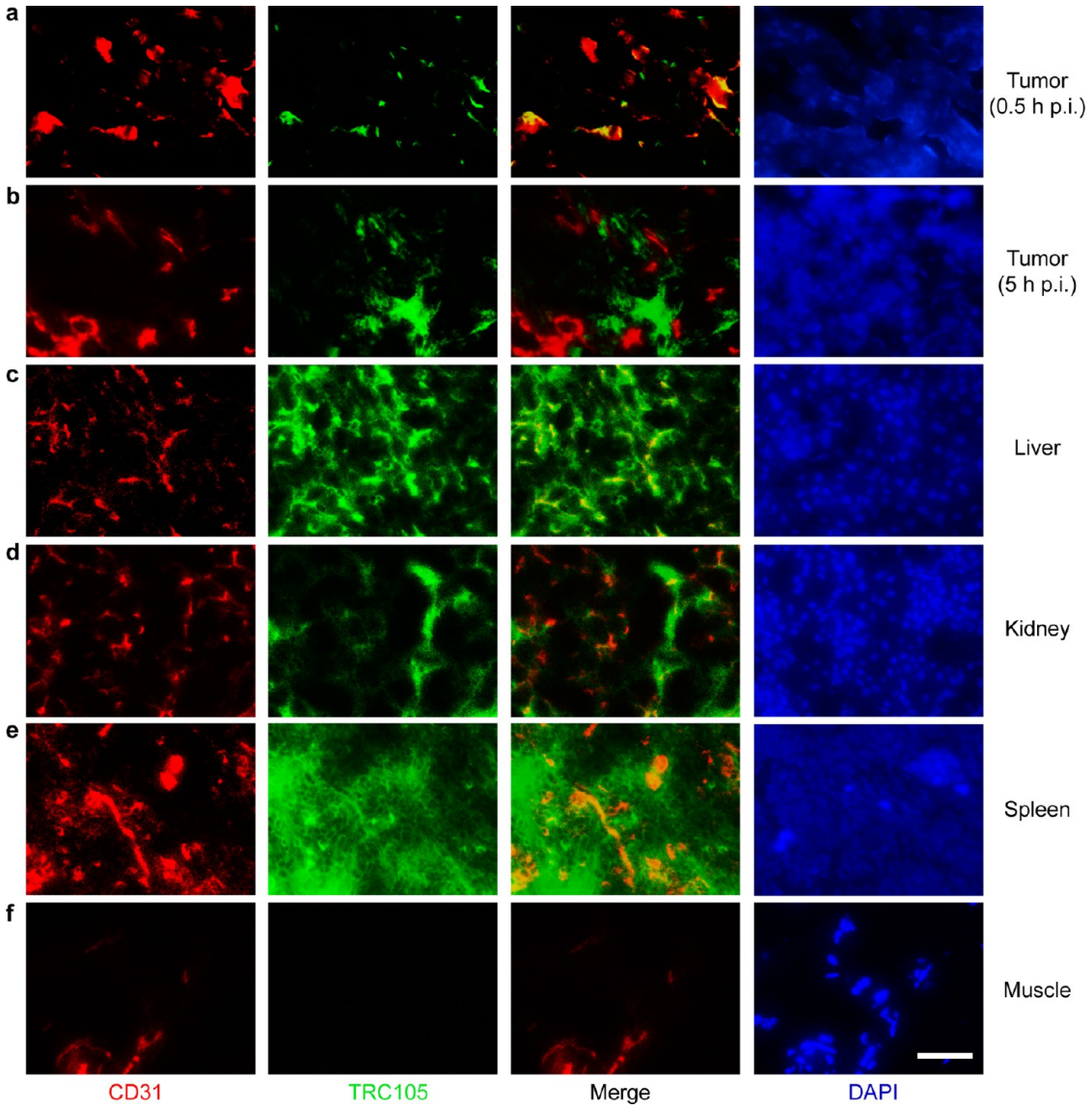

Figure 6. *Ex vivo* **histological analysis. (a) 4T1 tumor at 0.5 h p.i., (b) 4T1 tumor at 5 h p.i., (c) liver at 5 h p.i., (d) kidney at 5 h p.i., (e) spleen at 5 h p.i., (f) muscle at 5 h p.i. CD31 staining is shown in red, using an antimouse CD31 primary antibody. TRC105 within NOTA-mSiO_2-PEG-TRC105 was used as the primary antibody to indicate the location of the nanoconjugate (green). Merged images are also shown. DAPI staining was performed to reveal the location of the nuclei. Scale bar: 50 μm.**

Figure 7d. Half an hour after intravenous injection of NOTA-mSiO_2(DOX)-PEG-TRC105 and NOTA-mSiO_2-(DOX)-PEG into 4T1 tumor-bearing mice (dose: 78 μg of DOX per mouse, or 3.9 mg of DOX/kg of mouse body weight), the major organs were collected and imaged in an IVIS spectrum *in vivo* imaging system (excitation: 465 nm; emission: 580 nm), which is shown in Figure 7e. It is important to note that because of different absorption/scattering behaviors of various tissues, optical signal intensities from different organs may not accurately reflect the absolute uptake level of injected fluorescent agent/nanoparticle. For example, although liver is the dominant organ for NOTA-mSiO_2-PEG-TRC105 accumulation, as evidenced in our PET and biodistribution studies, only weak optical signal could be observed based on *ex vivo* optical imaging because of its dark color and strong absorbance of visible DOX fluorescence (Figure 7e). In contrast, due to the much lighter color of tumor tissue, strong optical signal from DOX could be observed in mice injected with NOTA-mSiO_2(DOX)-PEG-TRC105 (Figure 7e). Importantly, quantitative data from ROI analysis of the tumor tissue showed significantly higher fluorescent signal of DOX for NOTA-mSiO_2(DOX)-PEG-TRC105 (2.38×10^8 [p/s]/[μW/cm^2]), which is about 2-fold of that for NOTA-mSiO_2(DOX)-PEG (1.49×10^8 [p/s]/[μW/cm^2]), clearly demonstrating the feasibility to deliver larger amount of anticancer drugs to the tumor site *in vivo* by using TRC105-conjugated mSiO_2.

DISCUSSION

Successful surface modification of mSiO_2 is critical for achieving sufficient *in vivo* stability and efficient

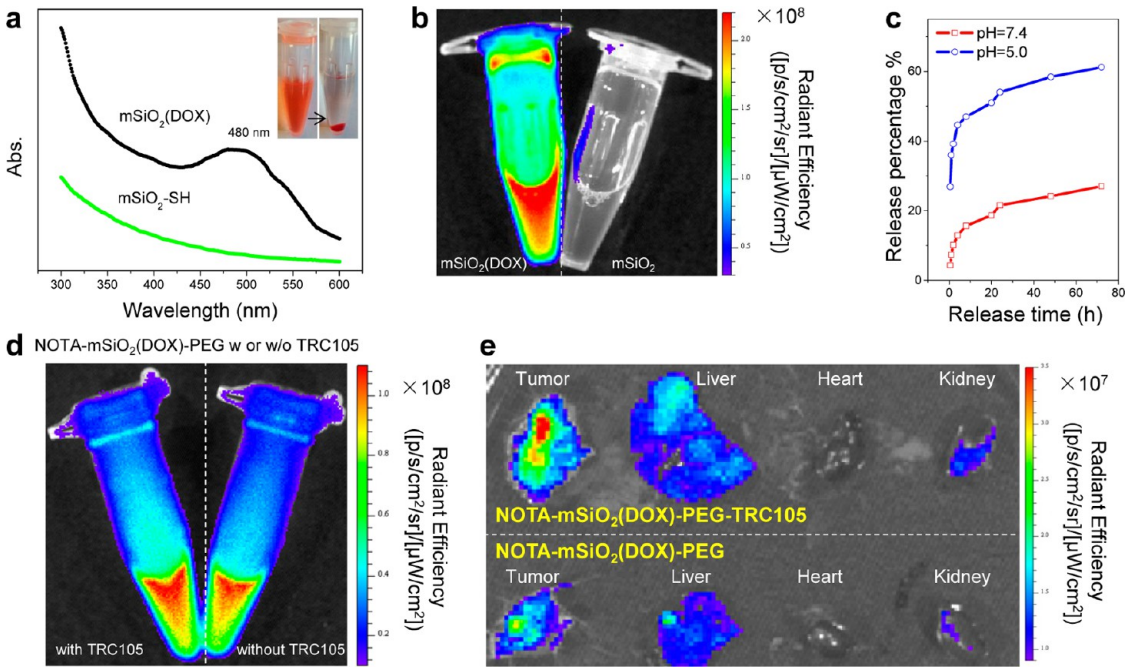

Figure 7. Enhanced tumor targeted drug delivery with NOTA-mSiO$_2$(DOX)-PEG-TRC105. (a) UV−vis spectra of mSiO$_2$−SH and mSiO$_2$(DOX) in aqueous solution. Inset shows that DOX is loaded inside the mSiO$_2$, rather than dissolved in the solution, which forms a color pellet after centrifugation. (b) Corresponding fluorescence images of mSiO$_2$(DOX) (emission at 580 nm) and mSiO$_2$ under the excitation of 465 nm light. (c) pH-sensitive release profiles of mSiO$_2$(DOX) at pH 5.0 and pH 7.4. (d) Fluorescence images (emission at 580 nm) of NOTA-mSiO$_2$(DOX)-PEG-TRC105 and NOTA-mSiO$_2$(DOX)-PEG in PBS solution (pH 7.4) under the excitation of 465 nm light. Both samples have the same DOX concentration of ~390 μg/mL. (e) An *ex vivo* optical image of major organs at 0.5 h after intravenous injection of NOTA-mSiO$_2$(DOX)-PEG-TRC105 (78 μg of DOX per mouse) or NOTA-mSiO$_2$(DOX)-PEG (78 μg of DOX per mouse) in 4T1 tumor-bearing mice, which clearly showed stronger tumor DOX signal in the former.

tumor targeted drug delivery. Surface thiolation of mSiO$_2$ is the first important step, which could be efficiently achieved by reacting MPS with mSiO$_2$ in absolute ethanol at 90 °C. The reaction temperature was found to be extremely important in this case, where simply refluxing the mixture at 78 °C for 24 h was found to be not sufficient. In our design, surface PEGylation was performed twice to facilitate orthogonal NOTA and TRC105 conjugation, as well as ensuring that the nanoparticles are stable in biological conditions and reducing the opsonization to improve the blood circulation lifetime of ^{64}Cu-NOTA-mSiO$_2$-PEG-TRC105 in mice. Our comprehensive characterizations (*e.g.*, TEM, DLS and zeta potential) confirmed the success of each surface modification step, and the final nanoconjugates could be well-dispersed in PBS without noticeable aggregation for weeks.

In vivo pharmacokinetics and biodistribution of mSiO$_2$ are very important issues to consider as a drug delivery system. Previously, although biodistribution of mSiO$_2$ in different organs could be investigated by covalently linked fluorescent dyes (*e.g.*, FITC) within or at the surface of mSiO$_2$,[16,38,39] such approach is not quantitative because of the qualitative nature of optical imaging. Quantitative biodistribution of mSiO$_2$ based on inductively coupled plasma mass spectrometry (ICP-MS) analysis of Si concentrations in organs could be a better technique, if background levels of Si in different organs have been accurately measured as references.[16,40,41] PET allows for serial noninvasive imaging and more accurate quantification of nanoparticle uptake in live subjects, which obviates the need to sacrifice large number of animals and minimizes inter-individual variations.[42,43] In our study, by labeling the surface functionalized mSiO$_2$ nanoparticles with ^{64}Cu ($t_{1/2}$: 12.7 h), we present the first example of using highly sensitive PET imaging to investigate the biodistribution and *in vivo* tumor targeting efficiency of mSiO$_2$. Since serum stability studies confirmed that more than 90% of radioactivity is bound to the nanoparticle after 48 h, such excellent stability of radiolabel on the nanoparticles ensured that the signal observed in PET truly reflects the distribution of ^{64}Cu-labeled mSiO$_2$ nanoparticles.

As evidenced by *in vivo* PET imaging and biodistribution studies, liver, intestine, kidney, spleen, and tumor are the primary organs for uptake of ^{64}Cu-NOTA-mSiO$_2$-PEG-TRC105. The prominent liver uptake at 5 and 48 h postinjection indicates that the excretion of ^{64}Cu-NOTA-mSiO$_2$-PEG-TRC105 is mainly *via* the hepatobiliary pathway. The decrease of liver uptake over time is possibly due to the slow excretion of ^{64}Cu-NOTA-mSiO$_2$-PEG and ^{64}Cu-NOTA-mSiO$_2$-PEG-TRC105 into the intestine, which is supported by the

biodistribution studies where significant intestine uptake was observed. Similar hepatobiliary excretion of dye-doped $mSiO_2$ has been reported in previous studies.[40] Although toxicity evaluation is not the focus of this study, and many previous reports have already demonstrated the excellent biocompatibility of $mSiO_2$ *in vivo*,[16,41] no acute toxicity was observed in this work throughout the study period.

Potential renal clearance of $mSiO_2$ is still under debate. For example, no detectable renal excretion and only dominant hepatobiliary excretion have been reported for $mSiO_2$ with particle sizes ranging from 45 to 130 nm.[40,44] However, an increasing number of reports have indicated either partial or sometimes primarily renal clearance of $mSiO_2$ with similar size and surface coatings,[16,39,41] indicating that size and surface charge may not be the only factors that govern the clearance of $mSiO_2$ nanoparticles. In our study, we provided indirect evidence from both biodistribution studies and histological examination that $mSiO_2$ conjugates did accumulate in the kidneys to a certain extent, where the uptake of ^{64}Cu-NOTA-$mSiO_2$-PEG-TRC105 was 7.2 ± 1.1 %ID/g at 5 h p.i. (n = 3, Figure 5). The presence of NOTA-$mSiO_2$-PEG-TRC105 in the kidneys was also confirmed by histology (Figure 6d). Although previous studies speculated a potential glomerular damage to be the reason for renal clearance,[45] the exact mechanism remains to be elucidated in the future.

Similar to other types of nanoparticles, intravenous administration of $mSiO_2$ will also face multiple biological boundaries as they travel to the targeted tissue/organs/cells, which could significantly reduce their chances for accumulation in the tumor site.[46] Although enhanced *in vivo* therapeutic effect of drug-loaded $mSiO_2$ has been reported by conjugating nanoparticles with targeting ligands such as folic acid or transferrin,[16,17,47] significant differences in tumor uptake of nanoparticles have not been demonstrated between the targeted and nontargeted groups in the literature. In this work, using TRC105 as the targeting ligand for CD105 that is almost exclusively expressed on the tumor vasculature, we demonstrated not only specific targeting of ^{64}Cu-NOTA-$mSiO_2$-PEG-TRC105 to the tumor vasculature *in vivo*, but also the enhanced capability for delivering anticancer drugs to the tumor site. The uptake of ^{64}Cu-NOTA-$mSiO_2$-PEG-TRC105 in the 4T1 tumor is time-dependent and peaked at 5.9 ± 0.4 %ID/g at 5h p.i., which is about 2-fold of that for ^{64}Cu-NOTA-$mSiO_2$-PEG. To the best of our knowledge, this is the first quantitative data showing the active and passive targeting efficiency of functionalized $mSiO_2$. The specific tumor targeting was also confirmed by blocking study and histology. The capability to deliver more DOX to the 4T1 tumor *in vivo* was demonstrated by *ex vivo* optical imaging, which showed significantly higher optical signal intensity of DOX in the targeted group than that of the nontargeted group. Semiquantitative analysis of the optical imaging data further confirmed a nearly 2-fold difference between the two groups, which is consistent with the PET results. Since $mSiO_2$ can be loaded with both hydrophobic and hydrophilic drugs, which can also allow for controlled release of these drugs with response to environmental changes (*e.g.*, pH, redox potential, temperature, *etc.*),[10] this work may open up a new avenue for image-guided drug delivery and targeted cancer therapy with significantly reduced potential side effects.

CONCLUSION

Herein we report the first example of active tumor targeting of uniform $mSiO_2$ *in vivo*, which was specific for CD105 and could be noninvasively quantified by PET imaging. ^{64}Cu-NOTA-$mSiO_2$-PEG-TRC105 exhibited excellent stability and target specificity, which was investigated through various *in vitro*, *in vivo*, and *ex vivo* experiments. Since the 4T1 tumor cells do not express CD105 but the tumor vasculature in the 4T1 tumor tissue express high level of CD105, the specific targeting in this work was exclusively vascular CD105-based with no cancer cell targeting involved. Vascular targeting led to ~2 fold enhancement of tumor uptake when compared to that of passive targeting alone based on the EPR effect. Hepatobiliary uptake/clearance was observed for these $mSiO_2$ nanoconjugates (both targeted and nontargeted), in addition to appreciable renal uptake/clearance. As a proof-of-concept, we also demonstrated the capability of enhanced tumor targeted delivery of DOX in 4T1 tumor-bearing mice upon intravenous injection, using TRC105 as the targeting ligand and $mSiO_2$ as the drug carrier, which holds great potential for future image-guided drug delivery and targeted cancer therapy.

METHODS

Materials. TRC105 was provided by TRACON Pharmaceuticals Inc. (San Diego, CA). *p*-SCN-Bn-NOTA was acquired from Macrocyclics, Inc. (Dallas, TX). FITC, hematoxylin staining solution, and Chelex 100 resin (50−100 mesh), tetraethyl orthosilicate (TEOS), triethylamine (TEA), MPS, hexadecyl trimethyl ammonium chloride (CTAC, 25 wt %) were purchased from Sigma-Aldrich (St. Louis, MO). AlexaFluor488- and Cy3-labeled secondary antibodies were purchased from Jackson Immunoresearch Laboratories, Inc. (West Grove, CA). PD-10 columns were purchased from GE Healthcare (Piscataway, NJ). Absolute ethanol, sodium chloride (NaCl), and doxorubicin hydrochloride (DOX) were purchased from Fisher Scientific. Mal-PEG_{5k}-NH_2 and Mal-PEG_{5k}-SCM were obtained from Creative PEGworks. Water and all buffers were of Millipore grade and pretreated with Chelex 100 resin to ensure that the aqueous solution was free of heavy metals. All chemicals were used as received without further purification.

Characterization. Transmission electron microscopy (TEM) images were obtained on a FEI T12 microscope operated at an

accelerating voltage of 120 kV. Standard TEM samples were prepared by dropping dilute products onto carbon-coated copper grids. Fourier transform infrared (FT-IR) spectra were obtained in the range of 650−3500 cm^{-1} using a Bruker Equinox 55/S FT-IR/NIR Spectrophotometer. Nitrogen adsorption−desorption isotherms were measured at 77 K using a Micromeritics ASAP 2020 system. The samples were pretreated under a vacuum at 393 K for 12 h. Surface areas were determined using the BET method. Pore size distribution data were collected by the BJH method of the desorption branch of the isotherm. Dynamic light scattering (DLS) and zeta potential analysis were performed on Nano-Zetasizer (Malvern Instruments Ltd.). Fluorescence images were acquired with a Nikon Eclipse Ti microscope.

Synthesis of Uniform 80 nm Sized $mSiO_2$ Nanoparticles. Procedures for the synthesis of $mSiO_2$ with a uniform diameter of ∼80 nm were similar as previously described in the literature.[35] In a typical synthesis, CTAC (2 g) and TEA (20 mg) were dissolved in 20 mL of high Q water and stirred at room temperature for 1 h. Afterward, 1.0 mL of TEOS was added rapidly and the resulting mixture was stirred for 1 h at 95 °C in a water bath. The mixture was then cooled down, collected by centrifugation, and washed with water and ethanol to remove residual reactants. Subsequently, the product was extracted for 24 h with a 1 wt % solution of NaCl in methanol at room temperature to remove the template CTAC. This process was carried out for at least 3 times to ensure complete removal of CTAC.

Synthesis of $mSiO_2$−SH. To functionalize the $mSiO_2$ surface with −SH groups, as-synthesized $mSiO_2$ nanoparticles were first dispersed in 20 mL of absolute ethanol, followed by adding 500 μL of MPS. The system was sealed and kept at 86−90 °C in a water bath for 12−24 h. Afterward, the mixture was centrifuged and washed with ethanol several times to remove the residual MPS. The $mSiO_2$−SH could be well-dispersed in water, and the concentration of thiol groups (nmol/mL) was measured using Ellman's agent and cysteine-based standard solutions.[24]

Synthesis of NOTA-$mSiO_2$-PEG-TRC105 and NOTA-$mSiO_2$(DOX)-PEG-TRC105. One milliliter of $mSiO_2$−SH (with 100 nmol of −SH groups) in water was PEGylated with Mal-PEG_{5k}-NH_2 (2 mg, 400 nmol) at room temperature. No detectable −SH groups could be found after the first PEGylation, suggesting that the $mSiO_2$-PEG-NH_2 nanoparticle surface was covered with PEG chains (∼100 nmol). The as-synthesized $mSiO_2$-PEG-NH_2 could be well-dispersed in PBS (pH 7.4). *p*-SCN-Bn-NOTA (∼45 nmol, 5 μL of 5 mg/mL solution in dimethyl sulfoxide) was subsequently reacted with $mSiO_2$-PEG-NH_2 at pH 8.5 to obtain NOTA-$mSiO_2$-PEG-NH_2. On the basis of the reaction efficiency, for each NOTA-$mSiO_2$-PEG-NH_2 there were ∼10 NOTA groups. Afterward, 5 mg (1000 nmol) of Mal-PEG_{5k}-SCM were added and reacted for another 1 h, resulting in NOTA-$mSiO_2$-PEG-Mal. No detectable $-NH_2$ groups could be found on the basis of the Kaiser test, suggesting there were only −Mal groups (∼90 nmol) at the surface of NOTA-$mSiO_2$-PEG-Mal. NOTA-$mSiO_2$-PEG-TRC105 could be obtained by reacting TRC105-SH (5 nmol) with NOTA-$mSiO_2$-PEG-Mal. For each $mSiO_2$ nanoconjugate, there were approximately 10 NOTA, 5 TRC105 and 190 PEG_{5k}. To synthesize FITC conjugated NOTA-$mSiO_2$-PEG-TRC105, ∼64 nmol of FITC and ∼45 nmol of *p*-SCN-Bn-NOTA in dimethyl sulfoxide were used together at pH 8.5−9, under the reaction condition similar as described above.

For the synthesis of NOTA-$mSiO_2$(DOX)-PEG-TRC105, the PEGylated $mSiO_2$ nanoparticles were first loaded with DOX by mixing $mSiO_2$-PEG-NH_2 with DOX in PBS solution under constant shaking for 24 h, which resulted in $mSiO_2$(DOX)-PEG-NH_2. Similar protocols were then used for NOTA and TRC105 conjugation. The final NOTA-$mSiO_2$(DOX)-PEG-TRC105 nanoconjugate was dispersed in PBS before subsequent studies.

Flow Cytometry and Fluorescence Microscopy. Cells were first harvested and suspended in cold PBS with 2% bovine serum albumin at a concentration of 5×10^6 cells/mL and then incubated with FITC conjugated $mSiO_2$-PEG-TRC105 or FITC conjugated $mSiO_2$-PEG for 15 (or 120) min at room temperature. The cells were washed three times with cold PBS and centrifuged for 5 min. Afterward, the cells were washed and analyzed using a BD FACSCalibur four-color analysis cytometer, which is equipped with 488 and 633 nm lasers (Becton-Dickinson, San Jose, CA) and FlowJo analysis software (Tree Star, Ashland, OR). "Blocking" experiment was also performed in cells incubated with the same amount of FITC conjugated $mSiO_2$-PEG-TRC105, where 500 μg/mL of unconjugated TRC105 was added to evaluate the CD105 specificity of FITC conjugated $mSiO_2$-PEG-TRC105. The cells were also examined under a Nikon Eclipse Ti microscope to validate the FACS results.

^{64}Cu Labeling and Serum Stability Studies. $^{64}CuCl_2$ (74−148 MBq) was diluted in 300 μL of 0.1 M sodium acetate buffer (pH 6.5) and added to NOTA-$mSiO_2$-PEG-TRC105 or NOTA-$mSiO_2$-PEG. The reaction was allowed to proceed at 37 °C for 30 min with constant stirring. ^{64}Cu-NOTA-$mSiO_2$-PEG-TRC105 and ^{64}Cu-NOTA-$mSiO_2$-PEG were purified using PD-10 columns with PBS as the mobile phase. The radioactivity fractions (typically between 3.5 and 4.5 mL, total of 1 mL) were collected for further *in vitro* and *in vivo* experiments. After 6 mL of PBS, the unreacted ^{64}Cu may start to elute from the column. The whole procedure of ^{64}Cu labeling and purification of the $mSiO_2$ nanoconjugates took 90 ± 10 min (n = 10).

For serum stability studies, ^{64}Cu-NOTA-$mSiO_2$-PEG-TRC105 and ^{64}Cu-NOTA-$mSiO_2$-PEG were incubated in complete mouse serum at 37 °C for up to 48 h (the time period investigated for serial PET imaging, which is about four half-lives of ^{64}Cu). Portions of the mixture were sampled at different time points and filtered through 100 kDa cutoff filters. The filtrates were collected, and the radioactivity was measured. The percentages of retained (*i.e.*, intact) ^{64}Cu on the $mSiO_2$-PEG conjugates (^{64}Cu-NOTA-$mSiO_2$-PEG-TRC105 or ^{64}Cu-NOTA-$mSiO_2$-PEG) were calculated using the equation [(total radioactivity − radioactivity in filtrate)/total radioactivity] × 100%.

4T1 Murine Breast Cancer Model. All animal studies were conducted under a protocol approved by the University of Wisconsin Institutional Animal Care and Use Committee. To generate the 4T1 tumor model, 4−5 week old female BALB/c mice were purchased from Harlan (Indianapolis, IN, USA), and tumors were established by subcutaneously injecting 2×10^6 cells, suspended in 100 μL of 1:1 mixture of RPMI 1640 and Matrigel (BD Biosciences, Franklin Lakes, NJ), into the front flank of mice. The tumor sizes were monitored every other day, and the animals were subjected to *in vivo* experiments when the tumor diameter reached 5−8 mm.

PET Imaging and Biodistribution Studies. PET and PET/CT scans at various time points p.i. using a microPET/microCT Inveon rodent model scanner (Siemens Medical SolutionsUSA, Inc.), image reconstruction, and ROI analysis of the PET data were performed similarly as described previously.[48,49] Quantitative PET data were presented as percentage injected dose per gram of tissue (%ID/g). Tumor-bearing mice were each injected with 5−10 MBq of ^{64}Cu-NOTA-$mSiO_2$-PEG-TRC105 or ^{64}Cu-NOTA-$mSiO_2$-PEG *via* tail vein before serial PET scans. Another group of three 4T1 tumor-bearing mice were each injected with 1 mg of unlabeled TRC105 at 1 h before ^{64}Cu-NOTA-$mSiO_2$-PEG-TRC105 administration to evaluate the CD105 specificity of ^{64}Cu-NOTA-$mSiO_2$-PEG-TRC105 *in vivo* (*i.e.*, blocking experiment).

After the last PET scans at 48 h p.i., biodistribution studies were carried out to confirm that the %ID/g values based on PET imaging truly represented the radioactivity distribution in tumor-bearing mice. In addition, another three 4T1 tumor-bearing mice were each intravenously injected with ^{64}Cu-NOTA-$mSiO_2$-PEG-TRC105 and euthanized at 5 h p.i. (when tumor uptake was at the peak based on PET results) for biodistribution studies. Mice were euthanized, and blood, 4T1 tumor, and major organs/tissues were collected and wet-weighed. The radioactivity in the tissue was measured using a gamma-counter (Perkin-Elmer) and presented as %ID/g (mean ± SD).

Histology. Frozen tissue slices of 7 μm thickness were fixed with cold acetone and stained for endothelial marker CD31, as described previously through the use of a rat antimouse CD31 antibody and a Cy3-labeled donkey antirat IgG.[24,32,36] The tissue slices were also incubated with 2 μg/mL of AlexaFluor488-labeled goat antihuman IgG for visualization of NOTA-$mSiO_2$-PEG-TRC105 (no unconjugated TRC105 was used for histology). All images were acquired with a Nikon Eclipse Ti microscope.

Conflict of Interest: The authors declare the following competing financial interest(s): Charles P. Theuer is an employee of TRACON. The other authors declare no competing financial interest.

Acknowledgment. This work is supported, in part, by the University of Wisconsin—Madison, the National Institutes of Health (NIBIB/NCI 1R01CA169365), the Department of Defense (W81XWH-11-1-0644), and the American Cancer Society (125246-RSG-13-099-01-CCE). The authors gratefully acknowledge Dr. James A. Dumesic and Dong Wang for their assistance with N_2 adsorption—desorption isotherms and pore size distribution measurement, as well as the Analytical Instrumentation Center of the School of Pharmacy at UW—Madison for obtaining IR spectra.

Supporting Information Available: TEM images, FT-IR spectra, detailed characterization of mesoporous silica nanoparticles after each step of reaction, flow cytometry analysis, size exclusion column chromatography profile of the final conjugate, serum stability studies, serial PET images of 4T1 tumor-bearing mice after intravenous injection of $^{64}CuCl_2$, uptake in different tissues at serial time points postinjection in each group based on PET imaging, and DOX loading studies. This material is available free of charge *via* the Internet at http://pubs.acs.org.

REFERENCES AND NOTES

1. Ho, D.; Sun, X.; Sun, S. Monodisperse Magnetic Nanoparticles for Theranostic Applications. *Acc. Chem. Res.* **2011**, *44*, 875–882.
2. Xia, Y.; Li, W.; Cobley, C. M.; Chen, J.; Xia, X.; Zhang, Q.; Yang, M.; Cho, E. C.; Brown, P. K. Gold Nanocages: From Synthesis to Theranostic Applications. *Acc. Chem. Res.* **2011**, *44*, 914–924.
3. Liu, Z.; Liang, X. J. Nano-Carbons as Theranostics. *Theranostics* **2012**, *2*, 235–237.
4. Yang, K.; Feng, L.; Shi, X.; Liu, Z. Nano-Graphene in Biomedicine: Theranostic Applications. *Chem. Soc. Rev.* **2013**, *42*, 530–547.
5. Chen, F.; Bu, W.; Zhang, S.; Liu, X.; Liu, J.; Xing, H.; Xiao, Q.; Zhou, L.; Peng, W.; Wang, L.; *et al.* Positive and Negative Lattice Shielding Effects Co-existing in Gd (III) Ion Doped Bifunctional Upconversion Nanoprobes. *Adv. Funct. Mater.* **2011**, *21*, 4285–4294.
6. Chen, F.; Zhang, S.; Bu, W.; Chen, Y.; Xiao, Q.; Liu, J.; Xing, H.; Zhou, L.; Peng, W.; Shi, J. A Uniform Sub-50 nm-Sized Magnetic/Upconversion Fluorescent Bimodal Imaging Agent Capable of Generating Singlet Oxygen by Using a 980 nm Laser. *Chemistry* **2012**, *18*, 7082–7090.
7. Pan, D. Theranostic Nanomedicine with Functional Nanoarchitecture. *Mol. Pharmacol.* **2013**, *10*, 781–782.
8. Chen, X.; Gambhir, S. S.; Cheon, J. Theranostic Nanomedicine. *Acc. Chem. Res.* **2011**, *44*, 841–841.
9. Lee, J. E.; Lee, N.; Kim, T.; Kim, J.; Hyeon, T. Multifunctional Mesoporous Silica Nanocomposite Nanoparticles for Theranostic Applications. *Acc. Chem. Res.* **2011**, *44*, 893–902.
10. Yang, P.; Gai, S.; Lin, J. Functionalized Mesoporous Silica Materials for Controlled Drug Delivery. *Chem. Soc. Rev.* **2012**, *41*, 3679–3698.
11. Tarn, D.; Ashley, C. E.; Xue, M.; Carnes, E. C.; Zink, J. I.; Brinker, C. J. Mesoporous Silica Nanoparticle Nanocarriers: Biofunctionality and Biocompatibility. *Acc. Chem. Res.* **2013**, *46*, 792–801.
12. Rosenholm, J. M.; Meinander, A.; Peuhu, E.; Niemi, R.; Eriksson, J. E.; Sahlgren, C.; Linden, M. Targeting of Porous Hybrid Silica Nanoparticles to Cancer Cells. *ACS Nano* **2009**, *3*, 197–206.
13. Ferris, D. P.; Lu, J.; Gothard, C.; Yanes, R.; Thomas, C. R.; Olsen, J. C.; Stoddart, J. F.; Tamanoi, F.; Zink, J. I. Synthesis of Biomolecule-Modified Mesoporous Silica Nanoparticles for Targeted Hydrophobic Drug Delivery to Cancer Cells. *Small* **2011**, *7*, 1816–1826.
14. Zhu, C. L.; Song, X. Y.; Zhou, W. H.; Yang, H. H.; Wen, Y. H.; Wang, X. R. An Efficient Cell-Targeting and Intracellular Controlled-Release Drug Delivery System Based on MSN-PEM-Aptamer Conjugates. *J. Mater. Chem.* **2009**, *19*, 7765–7770.
15. Tsai, C. P.; Chen, C. Y.; Hung, Y.; Chang, F. H.; Mou, C. Y. Monoclonal Antibody-Functionalized Mesoporous Silica Nanoparticles (MSN) for Selective Targeting Breast Cancer Cells. *J. Mater. Chem.* **2009**, *19*, 5737–5743.
16. Lu, J.; Liong, M.; Li, Z.; Zink, J. I.; Tamanoi, F. Biocompatibility, Biodistribution, and Drug-Delivery Efficiency of Mesoporous Silica Nanoparticles for Cancer Therapy in Animals. *Small* **2010**, *6*, 1794–1805.
17. Lu, J.; Li, Z.; Zink, J. I.; Tamanoi, F. *In Vivo* Tumor Suppression Efficacy of Mesoporous Silica Nanoparticles-Based Drug-Delivery System: Enhanced Efficacy by Folate Modification. *Nanomedicine* **2012**, *8*, 212–220.
18. Davis, M. E.; Chen, Z. G.; Shin, D. M. Nanoparticle Therapeutics: an Emerging Treatment Modality for Cancer. *Nat. Rev. Drug Discovery* **2008**, *7*, 771–782.
19. Hong, H.; Zhang, Y.; Sun, J.; Cai, W. Molecular Imaging and Therapy of Cancer with Radiolabeled Nanoparticles. *Nano Today* **2009**, *4*, 399–413.
20. Kim, J.; Kim, H. S.; Lee, N.; Kim, T.; Kim, H.; Yu, T.; Song, I. C.; Moon, W. K.; Hyeon, T. Multifunctional Uniform Nanoparticles Composed of a Magnetite Nanocrystal Core and a Mesoporous Silica Shell for Magnetic Resonance and Fluorescence Imaging and for Drug Delivery. *Angew. Chem., Int. Ed.* **2008**, *47*, 8438–8441.
21. Lee, J. E.; Lee, N.; Kim, H.; Kim, J.; Choi, S. H.; Kim, J. H.; Kim, T.; Song, I. C.; Park, S. P.; Moon, W. K.; *et al.* Uniform Mesoporous Dye-Doped Silica Nanoparticles Decorated with Multiple Magnetite Nanocrystals for Simultaneous Enhanced Magnetic Resonance Imaging, Fluorescence Imaging, and Drug Delivery. *J. Am. Chem. Soc.* **2010**, *132*, 552–557.
22. Meng, H.; Xue, M.; Xia, T.; Ji, Z.; Tarn, D. Y.; Zink, J. I.; Nel, A. E. Use of Size and a Copolymer Design Feature to Improve the Biodistribution and the Enhanced Permeability and Retention Effect of Doxorubicin-Loaded Mesoporous Silica Nanoparticles in a Murine Xenograft Tumor Model. *ACS Nano* **2011**, *5*, 4131–4144.
23. Shi, S.; Yang, K.; Hong, H.; Valdovinos, H. F.; Nayak, T. R.; Zhang, Y.; Theuer, C. P.; Barnhart, T. E.; Liu, Z.; Cai, W. Tumor Vasculature Targeting and Imaging in Living Mice with Reduced Graphene Oxide. *Biomaterials* **2013**, *34*, 3002–3009.
24. Hong, H.; Yang, K.; Zhang, Y.; Engle, J. W.; Feng, L.; Yang, Y.; Nayak, T. R.; Goel, S.; Bean, J.; Theuer, C. P.; *et al. In Vivo* Targeting and Imaging of Tumor Vasculature with Radiolabeled, Antibody-Conjugated Nanographene. *ACS Nano* **2012**, *6*, 2361–2370.
25. Xiao, Y.; Hong, H.; Javadi, A.; Engle, J. W.; Xu, W.; Yang, Y.; Zhang, Y.; Barnhart, T. E.; Cai, W.; Gong, S. Multifunctional Unimolecular Micelles for Cancer-Targeted Drug Delivery and Positron Emission Tomography Imaging. *Biomaterials* **2012**, *33*, 3071–3082.
26. Bergers, G.; Benjamin, L. E. Tumorigenesis and the Angiogenic Switch. *Nat. Rev. Cancer* **2003**, *3*, 401–410.
27. Folkman, J. Angiogenesis in Cancer, Vascular, Rheumatoid and Other Disease. *Nat. Med.* **1995**, *1*, 27–31.
28. Seon, B. K.; Haba, A.; Matsuno, F.; Takahashi, N.; Tsujie, M.; She, X.; Harada, N.; Uneda, S.; Tsujie, T.; Toi, H.; *et al.* Endoglin-Targeted Cancer Therapy. *Curr. Drug Delivery* **2011**, *8*, 135–143.
29. Fonsatti, E.; Nicolay, H. J.; Altomonte, M.; Covre, A.; Maio, M. Targeting Cancer Vasculature via Endoglin/CD105: a Novel Antibody-Based Diagnostic and Therapeutic Strategy in Solid Tumours. *Cardiovasc. Res.* **2010**, *86*, 12–19.
30. Dallas, N. A.; Samuel, S.; Xia, L.; Fan, F.; Gray, M. J.; Lim, S. J.; Ellis, L. M. Endoglin (CD105): a Marker of Tumor Vasculature and Potential Target for Therapy. *Clin. Cancer Res.* **2008**, *14*, 1931–1937.
31. Rosen, L. S.; Hurwitz, H. I.; Wong, M. K.; Goldman, J.; Mendelson, D. S.; Figg, W. D.; Spencer, S.; Adams, B. J.; Alvarez, D.; Seon, B. K.; *et al.* A Phase I First-in-Human Study of TRC105 (Anti-Endoglin Antibody) in Patients with Advanced Cancer. *Clin. Cancer Res.* **2012**, *18*, 4820–4829.
32. Hong, H.; Severin, G. W.; Yang, Y.; Engle, J. W.; Zhang, Y.; Barnhart, T. E.; Liu, G.; Leigh, B. R.; Nickles, R. J.; Cai, W. Positron Emission Tomography Imaging of CD105 Expression with ^{89}Zr-Df-TRC105. *Eur. J. Nucl. Med. Mol. Imaging* **2012**, *39*, 138–148.
33. Hong, H.; Yang, Y.; Zhang, Y.; Engle, J. W.; Barnhart, T. E.; Nickles, R. J.; Leigh, B. R.; Cai, W. Positron Emission

Tomography Imaging of CD105 Expression during Tumor Angiogenesis. *Eur. J. Nucl. Med. Mol. Imaging* **2011**, *38*, 1335–1343.
34. Hong, H.; Zhang, Y.; Severin, G. W.; Yang, Y.; Engle, J. W.; Niu, G.; Nickles, R. J.; Chen, X.; Leigh, B. R.; Barnhart, T. E.; *et al.* Multimodality Imaging of Breast Cancer Experimental Lung Metastasis with Bioluminescence and a Monoclonal Antibody Dual-Labeled with ^{89}Zr and IRDye 800CW. *Mol. Pharm.* **2012**, *9*, 2339–2349.
35. Pan, L.; He, Q.; Liu, J.; Chen, Y.; Ma, M.; Zhang, L.; Shi, J. Nuclear-Targeted Drug Delivery of TAT Peptide-Conjugated Monodisperse Mesoporous Silica Nanoparticles. *J. Am. Chem. Soc.* **2012**, *134*, 5722–5725.
36. Hong, H.; Zhang, Y.; Engle, J. W.; Nayak, T. R.; Theuer, C. P.; Nickles, R. J.; Barnhart, T. E.; Cai, W. *In Vivo* Targeting and Positron Emission Tomography Imaging of Tumor Vasculature with ^{66}Ga-Labeled Nano-Graphene. *Biomaterials* **2012**, *33*, 4147–4156.
37. Yuan, L.; Tang, Q.; Yang, D.; Zhang, J. Z.; Zhang, F.; Hu, J. Preparation of pH-Responsive Mesoporous Silica Nanoparticles and Their Application in Controlled Drug Delivery. *J. Phys. Chem. C* **2011**, *115*, 9926–9932.
38. Almeida, J. P. M.; Chen, A. L.; Foster, A.; Drezek, R. *In Vivo* Biodistribution of Nanoparticles. *Nanomedicine* **2011**, *6*, 815–835.
39. He, X.; Nie, H.; Wang, K.; Tan, W.; Wu, X.; Zhang, P. *In Vivo* Study of Biodistribution and Urinary Excretion of Surface-Modified Silica Nanoparticles. *Anal. Chem.* **2008**, *80*, 9597–9603.
40. Souris, J. S.; Lee, C. H.; Cheng, S. H.; Chen, C. T.; Yang, C. S.; Ho, J. A.; Mou, C. Y.; Lo, L. W. Surface Charge-Mediated Rapid Hepatobiliary Excretion of Mesoporous Silica Nanoparticles. *Biomaterials* **2010**, *31*, 5564–5574.
41. Fu, C.; Liu, T.; Li, L.; Liu, H.; Chen, D.; Tang, F. The Absorption, Distribution, Excretion and Toxicity of Mesoporous Silica Nanoparticles in Mice Following Different Exposure Routes. *Biomaterials* **2013**, *34*, 2565–2575.
42. Holland, J. P.; Cumming, P.; Vasdev, N. PET Radiopharmaceuticals for Probing Enzymes in the Brain. *Am. J. Nucl. Med. Mol. Imaging* **2013**, *3*, 194–216.
43. Nolting, D. D.; Nickels, M. L.; Guo, N.; Pham, W. Molecular Imaging Probe Development: a Chemistry Perspective. *Am. J. Nucl. Med. Mol. Imaging* **2012**, *2*, 273–306.
44. Kumar, R.; Roy, I.; Ohulchanskky, T. Y.; Vathy, L. A.; Bergey, E. J.; Sajjad, M.; Prasad, P. N. *In Vivo* Biodistribution and Clearance Studies Using Multimodal Organically Modified Silica Nanoparticles. *ACS Nano* **2010**, *4*, 699–708.
45. Yu, T.; Greish, K.; McGill, L. D.; Ray, A.; Ghandehari, H. Influence of Geometry, Porosity, and Surface Characteristics of Silica Nanoparticles on Acute Toxicity: Their Vasculature Effect and Tolerance Threshold. *ACS Nano* **2012**, *6*, 2289–2301.
46. Nichols, J. W.; Bae, Y. H. Odyssey of a Cancer Nanoparticle: from Injection Site to Site of Action. *Nano Today* **2012**, *7*, 606–618.
47. Liu, H.; Liu, T.; Wu, X.; Li, L.; Tan, L.; Chen, D.; Tang, F. Targeting Gold Nanoshells on Silica Nanorattles: a Drug Cocktail to Fight Breast Tumors via a Single Irradiation with Near-Infrared Laser Light. *Adv. Mater.* **2012**, *24*, 755–761.
48. Zhang, Y.; Hong, H.; Engle, J. W.; Yang, Y.; Barnhart, T. E.; Cai, W. Positron Emission Tomography and Near-Infrared Fluorescence Imaging of Vascular Endothelial Growth Factor with Dual-Labeled Bevacizumab. *Am. J. Nucl. Med. Mol. Imaging* **2012**, *2*, 1–13.
49. Hong, H.; Benink, H. A.; Uyeda, H. T.; Valdovinos, H. F.; Zhang, Y.; Meisenheimer, P.; Barnhart, T. E.; Fan, F.; Cai, W. HaloTag as a Reporter Gene: Positron Emission Tomography Imaging with ^{64}Cu-Labeled Second Generation HaloTag Ligands. *Am. J. Transl. Res.* **2013**, *5*, 291–302.